Chapter 2
Principles of Transport in Multicomponent Plasmas

Igor D. Kaganovich, Raoul N. Franklin, and Vladimir I. Demidov

Abstract The main principles of transport in multicomponent plasmas are described. Because the bulk plasma is charged positively to keep electrons together with positive ions, negative ions are confined by electrostatic fields inside the plasma and they flow from the plasma periphery toward the center. It is shown that the flow velocity of negative ions is a nonlinear function of the negative ion density. Increasing the negative ion density makes the electron density profile flatter and leads to a decrease of the electric field. Such a nonlinear dependence of the negative ion flow velocity on their density results in the formation of steep gradients of negative ion density, or negative ion fronts. Addition of negative ions makes the plasma afterglow a complex process as well. Typically, two stages of afterglow appear. In the first stage, the negative ions are trapped inside the plasma and only electrons and positive ions can reach the walls. However, at a later time, electrons quickly leave the plasma, and the second stage of afterglow begins, in which electrons are totally absent and an ion–ion plasma forms. During this stage, only the negative and positive ions contribute to the wall fluxes. The complex structure of the radio frequency sheath in strongly electronegative gases is also reviewed. Similar phenomena are observed in dusty plasmas. A possible relevance to ball lightning is discussed.

I.D. Kaganovich (✉)
Plasma Physics Laboratory, Princeton University, NJ 08543, USA
e-mail: ikaganov@ppppl.gov

R.N. Franklin
Department of Physics and Astronomy, The Open University,
Milton Keynes MK7 6AA, UK
e-mail: r.n.franklin@open.ac.uk

V.I. Demidov
UES, Inc., Dayton-Xenia Rd., Beavercreek, Ohio 45432, USA
and
Department of Physics, West Virginia University, Morgantown, WV 26506
e-mail: demidov@wvu.edu

M. Bonitz et al. (eds.), *Introduction to Complex Plasmas*, Springer Series on Atomic, Optical, and Plasma Physics 59, DOI 10.1007/978-3-642-10592-0_2,

2.1 Introduction

Most elements of the periodic table produce negative ions. Table 2.1 shows the electron affinity of elements for the formation of negative ions. The larger the electron affinity, the easier it is to form a negative ion. From Table 2.1, it is evident that elements of the groups 6 and 7 have a large electron affinity of the order of a few electron volts and thus most readily produce negative ions. Halogen gases of the group 7, most importantly chlorine and fluorine, are frequently used in the semiconductor industry for dry-etching processes [3] and elimination of notching [4]. The creation of negative ions in oxygen plasmas is an important process in atmospheric electricity and in the formation of the ionospheric D-layer [5]. The production and acceleration of hydrogen or deuterium negative ions are utilized for generating powerful neutral beams to heat and drive current in magnetically confined plasmas for fusion energy research [6]. Negative ion beams made from halogens were also proposed as potential drivers for heavy ion fusion [7].

This review aims at introducing a general reader to the qualitative effects in plasma transport arising from the addition of negative ions. Given the fact that the chapter is limited in size, only the most important and robust effects are described. Further details can be found in cited literature. The organization of the chapter is as follows. Section 2.1.1 describes the production and destruction mechanisms of negative ions. Section 2.1.2 derives the drift–diffusion approximation describing plasma transport. Section 2.2 briefly reminds the reader about ambipolar diffusion to prepare for Sect. 2.3 on the more complicated temporal dynamics of negative ion flows in multicomponent plasmas. Section 2.4 describes the various stages of afterglow in multicomponent plasmas and wall fluxes of negative ions. General properties of steady-state profiles of plasmas with negative ions are reviewed in Sect. 2.5. Section 2.6 is devoted to a very interesting example of influence of negative ions on the rf-sheath structure in strongly electronegative gases. And last, but not least, Sect. 2.7 shows the relevance of the described phenomena associated with negative ions to dusty plasmas and ball lightning.

Table 2.1 Electron affinity, E_f, for formation of negative ions (from [1, 2])

Group period	I	II	III	IV	V	VI	VII	VIII
1	H 0.75							He 0.075[a]
2	Li 0.62	Be 0.004[a]	B 0.28	C 1.2	N 0.2[a]	O 1.45	F 3.4	Ne 0.095[a]
3	Na 0.54	Mg 0.004[a]	Al 0.44	Si 1.4	P 0.75	S 2.08	Cl 3.61	Ar 0.17[a]
4	K 0.5	Ca 0.02	Sc 0.19	Ge 1.2	As 0.81	Se 2.02	Br 3.36	Kr 0.65[a]
5	Rb 0.49	Ba 0.15	Sr 0.11	Sn 1.1	Sb 1.1	Te 1.97	I 3.06	Xe 1.25[a]
6	Cs 0.47	Ra	Ba 0.15	Pb 0.36	Bi 0.95	Po 1.9	At 2.8	Rn

[a]Metastable negative ions; their lifetime is typically a fraction of ms.

2.1.1 Production and Destruction Mechanisms of Negative Ions

Production of negative ions occurs in a number of processes [1–3]:

Electron attachment.

$$e + A \rightarrow A^-$$

An electron attaches to an atom A and the released energy of the electron affinity, E_f, transfers to photons or to a third body.

Dissociative attachment.

$$e + AB(^*) \rightarrow A^- + B$$

An electron attaches to a molecule AB, often in an excited state and the energy of the electron affinity and excitation, $E_f - E^*$, is absorbed in dissociation of the molecule.

Charge transfer.

$$A^- + B \rightarrow A + B^-$$

An electron is transferred from a negative ion A^- to another atom B.

Clustering reactions.

$$A^- + B + C \rightarrow AB^- + C$$

Negative ions often play an important role in the formation of a cluster, as an initial seed of a clustering reaction (see, e.g., [8]).

Destruction of negative ions occurs due to following processes [1–3]:

Electron detachment.

$$e + A^- \rightarrow A + 2e; \quad e + AB^- \rightarrow A + B + 2e$$

An electron impacts a negative ion, which leads to "ionization" of the negative ion, in which a loosely bound electron detaches from the negative ion.

Associative detachment.

$$A^- + B \rightarrow AB + e$$

A collision of a negative ion with an atom yields the formation of a molecule; the difference between the dissociation energy and the electron affinity is transferred to a free electron.

Charge transfer.

$$A^- + B \rightarrow A + B^-$$

An electron is transferred from a negative ion A^- to another atom B.

Positive ion–negative ion recombination.

$$A^- + B^+ \rightarrow A + B^*$$

A collision of a negative ion with a positive ion leads to recombination of ions.

At high pressures, three-body recombination between electron and ion in the presence of a third atom can become important.

A detailed description of the formation of negative ions must therefore include a set of several reactions between neutrals, positive and negative ions, and molecules. In many cases, the formation of metastable states of atoms or even vibrationally excited molecules makes it important to take these processes into account for a correct description of negative ion creation. For commonly used gases such as oxygen, chlorine, silane, and sulfur hexafluoride (SF_6), such sets of participating reactions have been developed and tested against experimental measurements [3,9]. For many other gas mixtures, it remains a difficult task to determine all of the possible routes for negative ion formation and destruction.

2.1.2 *The Drift–Diffusion Approximation for the Description of Plasma Transport*

Most plasma devices utilizing negative ions operate in discharge chambers and at pressures large enough to be able to produce a sufficient amount of negative ions. Therefore, the ion mean free path is typically small compared with the discharge chamber dimensions and ion transport can be described making use of the drift–diffusion equations [3,10–12]. For discussion of effects in collisionless plasma, see, for example, [13–16]. The momentum balance for the positive ions with density, n_p, and temperature, T_i, reads

$$-\nabla n_p T_i + e n_p \mathbf{E} - M_{pa} n_p \nu_{ia} \mathbf{u}_p = 0. \tag{2.1}$$

Here, we have neglected the ion inertia term, which is small compared to the ion friction term, $M_{pa} n_p \nu_{pa} \mathbf{u}_p$, based on the assumption of small mean free path. Here, M_{pa} is the reduced mass of the positive ion and gas atom [10]. If the mean ion–neutral atom collision frequency, ν_{pa}, can be assumed independent of the mean ion flow velocity, $\mathbf{u}_p$, the ion flux can be expressed as

$$\Gamma_p = n_p \mathbf{u}_p = \frac{-\nabla n_p T_i + e n_p \mathbf{E}}{M_{pa} n_p \nu_{pa}} = \frac{-T_i \nabla n_p + e n_p \mathbf{E}}{M_{pa} n_p \nu_{pa}}. \tag{2.2}$$

The assumption of the collision frequency, ν_{pa}, being independent of the mean ion flow velocity, $\mathbf{u}_p$, requires that the ion mean flow velocity be small compared with the ion thermal velocity, which may fail in the limit of low pressures [3]. Nevertheless, accounting for the variable collision frequency, $\nu_{pa}(u_p)$ does not change results qualitatively, but makes analytic results less transparent. Corresponding results can be easily generalized for the case of the variable collision frequency (see, e.g., [3, 17]). Therefore, in the following, we assume that ν_{pa} is independent of the mean ion flow velocity and utilize drift–diffusion equations. Similarly, in (2.2) we assumed that the ion temperature is constant. This is not accurate due to gas heating by the discharge current (see, e.g., [11,18]). Likewise, it is not important to take this effect into account to examine qualitative effects described in this chapter.

Equation (2.2) is traditionally rewritten in the form of drift–diffusion equation:

$$\Gamma_{\mathrm{p}} = -D_{\mathrm{p}} \nabla n_{\mathrm{p}} + e n_{\mathrm{p}} \mu_{\mathrm{p}} E, \tag{2.3}$$

where

$$D_{\mathrm{p}} = \frac{T_{\mathrm{i}}}{M_{\mathrm{pa}} \nu_{\mathrm{pa}}} = \frac{v_{T_{\mathrm{i}}}^2}{\nu_{\mathrm{pa}}} = \frac{v_{T_{\mathrm{i}}}^2}{\nu_{\mathrm{pa}}^2} \nu_{\mathrm{pa}} = \lambda_{\mathrm{pa}}^2 \nu_{\mathrm{pa}}$$

is the ion diffusion coefficient and $\mu_{\mathrm{p}} = e/M_{\mathrm{pa}} \nu_{\mathrm{pa}}$ is the positive ion mobility. Here, $v_{T_{\mathrm{i}}} = \sqrt{T_{\mathrm{i}}/M_{\mathrm{pa}}}$ is the ion thermal velocity.

Similarly, the negative ion flux can be expressed as a function of negative ion density and its gradients, n_{n}, as

$$\Gamma_{\mathrm{n}} = -D_{\mathrm{n}} \nabla n_{\mathrm{n}} - e n_{\mathrm{n}} \mu_{\mathrm{n}} E, \tag{2.4}$$

where $D_{\mathrm{n}} = T_{\mathrm{i}}/M_{\mathrm{n}} \nu_{\mathrm{na}}$ is the ion diffusion coefficient and $\mu_{\mathrm{n}} = e/M_{\mathrm{n}} \nu_{\mathrm{na}}$ is the negative ion mobility. Here, M_{na} is the reduced mass of the negative ion gas and atom and ν_{pa} is the mean negative ion–neutral atom collision frequency.

Finally, the electron flux is determined from

$$\Gamma_{\mathrm{e}} = -D_{\mathrm{e}} \nabla n_{\mathrm{e}} - e n_{\mathrm{e}} \mu_{\mathrm{e}} E, \tag{2.5}$$

where $D_{\mathrm{e}} = T_{\mathrm{e}}/m \nu_{\mathrm{ea}}$ is the electron diffusion coefficient and $\mu_{\mathrm{e}} = e/m \nu_{\mathrm{ea}}$ is the electron mobility, m is the electron mass and T_{e} is the electron temperature. Note that in accord with the Einstein relation for each species k, the diffusion coefficient is equal to the product of the mobility and the species temperature $D_k = \mu_k T_k$ [10].

2.2 Ambipolar Diffusion

Let us start by briefly describing the transport of a two-component plasma without negative ions. The electron density is determined from the continuity equation:

$$\frac{\partial n_{\mathrm{e}}}{\partial t} = -\frac{\partial}{\partial x} \left(-D_{\mathrm{e}} \frac{\partial n_{\mathrm{e}}}{\partial x} - e n_{\mathrm{e}} \mu_{\mathrm{e}} E \right) + S_{\mathrm{e}}, \tag{2.6}$$

where S_{e} is the total volumetric electron production rate, which is sum of the source and loss terms for electron production. Typically, the term associated with electron diffusion is much larger than any source terms and electrons diffuse away from the positive ions until the plasma polarizes and the electric field stops the electron flux, as shown in Fig. 2.1 [3, 10–12]

$$\Gamma_{\mathrm{e}} = -D_{\mathrm{e}} \frac{\partial n_{\mathrm{e}}}{\partial x} - e n_{\mathrm{e}} \mu_{\mathrm{e}} E \approx 0. \tag{2.7}$$

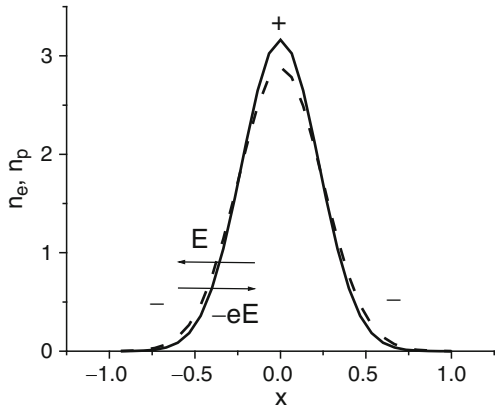

Fig. 2.1 Plasma polarization during ambipolar diffusion

Phenomena associated with current-carrying plasma are described in [12]. A zero electron flux corresponds to the electrons obeying a Boltzmann relation, that is, the electric field is determined by

$$eE = \frac{-D_e \nabla n_e}{\mu_e n_e} \approx -T_e \frac{\nabla n_e}{n_e}. \tag{2.8}$$

Substituting (2.8) into the continuity equation for the positive ion density

$$\frac{\partial n_p}{\partial t} = -\frac{\partial}{\partial x}\left(-D_p \frac{\partial n_p}{\partial x} + e n_p \mu_p E\right) + S_p \tag{2.9}$$

yields the ambipolar diffusion equation

$$\frac{\partial n_p}{\partial t} = \frac{\partial}{\partial x}\left(\mu_p (T_e + T_p) \frac{\partial n_p}{\partial x}\right) + S_p. \tag{2.10}$$

Note that we have used the quasineutrality condition, $n_e = n_p$, to derive (2.10). The ambipolar diffusion equation (2.10) shows that the ambipolar diffusion rate is increased by a factor $(T_e/T_i + 1)$ compared with that of the ion diffusion due to plasma polarization and ion acceleration in the self-consistent electric field. The important property of the ambipolar diffusion equation (2.10) is that it is linear, thus describing relatively simple linear dynamics of the initially complex, nonlinear drift–diffusion equations (2.6) and (2.9). Any change of the indicated assumptions will result in restoring nonlinear effects contained initially in the nonlinear drift–diffusion description of (2.6) and (2.9) [12, 19]. For example, addition of negative ions results in a significant change of plasma transport, in which the simple concept of ambipolar diffusion is no longer valid [12, 20, 21].

2.3 Temporal Dynamics of Negative Ion Flows in Multicomponent Plasmas

As shown in the previous section, electrons achieve a Boltzmann equilibrium distribution as long as electron diffusion is much larger than the electron production terms, $|\partial\Gamma_e/\partial x| \gg |S_e|$. Because electrons are trapped by the self-consistent electric field, any negatively charged particle is pulled by the electric field from the discharge periphery into the plasma center. Substituting (2.8) into the continuity equation for the negative ions yields

$$\frac{\partial n_n}{\partial t} = -\frac{\partial}{\partial x}\left(-D_n\frac{\partial n_n}{\partial x} + e\mu_n T_e\frac{n_n}{n_e}\frac{\partial n_e}{\partial x}\right) + S_n. \tag{2.11}$$

In typical discharge conditions, the ion diffusion coefficient, $D_n = \mu_n T_i$, is small compared with $\mu_n T_e$, because the electron temperature is large compared with the ion temperature:

$$T_e \gg T_i \tag{2.12}$$

(ions are cooled in collisions with neutral atoms much faster than electrons, which in contrast to ions only lose a small portion of their energy, proportional to m/M). Therefore, a convective term, $\mu_n eEn_n$, dominates the dynamics of negative ions, unless the electron profile becomes very flat. Figure 2.2 shows the evolution of plasma profiles at the beginning of the active phase of the pulsed discharge in oxygen [22, 23]. The initial condition of the plasma at the beginning of the active glow corresponds to the final condition at the end of the afterglow of the previous pulse. For the chosen set of parameters, this corresponds to an ion–ion plasma with smooth

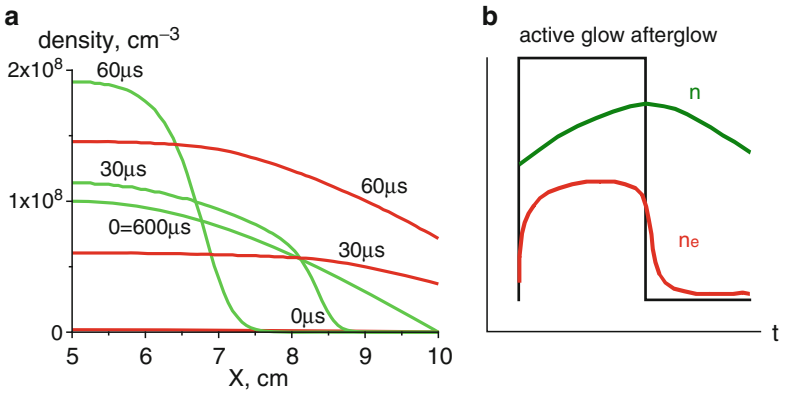

Fig. 2.2 Evolution of electron and negative ion densities in early active glow of a pulsed discharge. (**a**) Negative ion (*green lines*) and electron density (*red lines*) in the early active glow of Ar and 3% O_2 plasma. Interelectrode gap: 10 cm; total pressure: 5 mTorr; averaged power density: 1.0 mW/cm^3; pulse duration: 600 ms; duty ratio: 0.5; and *numbers* denote time in the active glow in μs. (**b**) Time evolution of the electron and negative ion density in the center of the discharge

cosine-like profiles of charged species densities (lines for 0 ms). Once the power is switched on (at time $t = 0$), the electron temperature rises to several eV. Because the electric field increases with the electron temperature, negative ions are squeezed toward the center of the plasma. However, as is evident from Fig. 2.2, the electron density gradient is much larger at the periphery of the discharge than in the center, indicating that negative ions move much faster at the periphery than in the center. Because negative ions slow down more rapidly in the densest part of the discharge, their density rises and can eventually lead to formation of large negative ion density gradients or negative ion density fronts. At the same time, because the negative ions are swept from the periphery region quickly, their density is low near discharge walls, where an electropositive plasma of mostly electrons and positive ions forms. *Thus, plasmas with negative ions tend to self-separate into two distinct regions: a region of electropositive plasma where the electric field is high and the negative ion density is small compared to the electron density, and an electronegative region where the negative ion density is large compared to the electron density and the electric field is weak* [24–31]. Such separation is completely contrary to the prediction of the second law of thermodynamics where mixing of all species is expected. This occurs due to the large difference between the electron and ion temperatures in low-temperature plasmas.

The formal description of the separation effect is not straightforward. To describe the flattening of the electron density gradient in the self-consistent evolution of plasma profiles in the presence of negative ions, we derive an effective equation for the electrons by subtracting the equation for the negative ions (2.11) from the equation for the positive ions (2.10), neglecting source and ion diffusion terms, where

$$\frac{\partial n_e}{\partial t} = \frac{\partial}{\partial x}\left(eT_e \frac{\mu_n n_n + \mu_p n_p}{n_e}\frac{\partial n_e}{\partial x}\right). \tag{2.13}$$

From (2.13), it is evident that the effective coefficient of electron diffusion,

$$D_{\text{eff}}\left(\frac{n}{n_e}\right) = eT_e \frac{\mu_n n_n + \mu_p n_p}{n_e} = \mu_p eT_e + eT_e(\mu_n + \mu_p)\frac{n_n}{n_e}, \tag{2.14}$$

is a strongly nonlinear function of the negative ion density and electronegativity, n_n/n_e. The larger the ratio of the negative ion density to the electron density, the larger is the effective diffusion coefficient. Given that changes in the electron flux, $\Gamma_e = -D_{\text{eff}}(\partial n_e/\partial x)$, are of the order of unity in the discharge, whereas the electronegativity, n_n/n_e, can change by large factors, the increase of the electronegativity eventually leads to a flattening of the electron density profile and a reduction of the electric field. Substituting the electron flux, $\Gamma_e = -D_{\text{eff}}(\partial n_e/\partial x)$, instead of the electron density into the equation for negative ions, (2.11) yields

$$\frac{\partial n_n}{\partial t} = -\frac{\partial}{\partial x}\Gamma_n \approx -u_{\text{eff}}\left(\frac{n_n}{n_e}\right)\frac{\partial}{\partial x}n_n, \tag{2.15}$$

where we have neglected the variation in the electron flux and density compared with those of the negative ions. Here, $\Gamma_n = -\Gamma_e[\mu_n n_n/(\mu_n n_n + \mu_p n_p)]$ and $u_{eff} = \partial\Gamma_n/\partial n_n$ are the negative ion signal propagation velocity [32]:

$$u_{eff} = \frac{\mu_n \mu_p T_e}{\mu_n n_n + \mu_p n_p} \frac{\partial n_e}{\partial x} = \frac{\mu_p n_e}{\mu_n n_n + \mu_p n_p} u_n. \tag{2.16}$$

From (2.16), it is evident that the velocity of propagation of the negative ion density perturbation is different from the velocity of negative ions, $u_n = \mu_n eE$. In the case when positive and negative ion mobilities coincide, the perturbation velocity is a factor of $2n_n/n_e + 1$, smaller than the negative ion velocity:

$$u_{eff} = \frac{1}{2n_n/n_e + 1} u_n. \tag{2.17}$$

If the negative ion density is small compared with the electron density, both velocities coincide, $u_{eff} = u_n$. However, if the negative ion density is large compared with the electron density, the signal propagation velocity is much smaller than the velocity of the negative ions, because the electron density gradient is strongly affected by the negative ion density changes. This effect was verified in numerical simulations [33] and is shown in Fig. 2.3, where the propagation of a small perturbation of negative ion density for three different cases of electronegativity and the same profile of initial electron density are shown. As is evident from Fig. 2.3, the propagation velocity for the case (b) $n_n/n_e \cong 1$ is about three times smaller than in case $n_n/n_e = 0$, in accord with (2.17).

The nonlinear evolution of a large negative ion density perturbation is shown in Fig. 2.4. The general theory of one-dimensional flows [34] predicts that each point of initial profile $n_n(x)$ moves with its own velocity $u_{eff}(n_n/n_e)$. According to

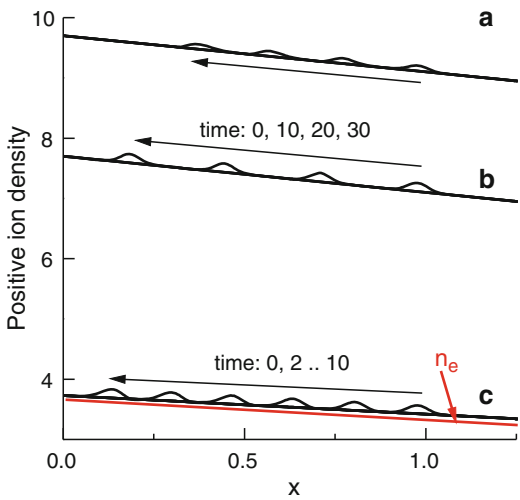

Fig. 2.3 Propagation of small perturbation of negative ion density for three different values of electronegativity n_n/n_e: (**a**) $n_n/n_e \cong 1.5$, (**b**) $n_n/n_e \cong 1$, and (**c**) $n_n/n_e = 0$, with the same profile of the initial electron density, $n_e = n_0(3.7 - 0.3x)$. All variables are dimensionless, normalized to reference values; density n/n_0, coordinate x/L, and time $t\mu_n T_e/L^2$. Ion diffusion is neglected and ion mobilities were assumed to be the same $\mu_n = \mu_p$

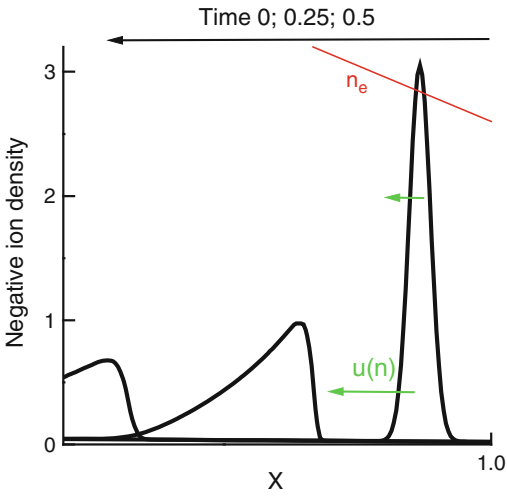

Fig. 2.4 Formation of negative ion density fronts during propagation of a large perturbation of negative ion density for the conditions of Fig. 2.3, but with $T_i/T_e = 10^{-3}$ and $n_e = n_0(6.2 - 3.6x)$. The negative ion density profiles are plotted three times every 0.25 units of dimensionless time $tL^2/\mu_n T_e$ [33]

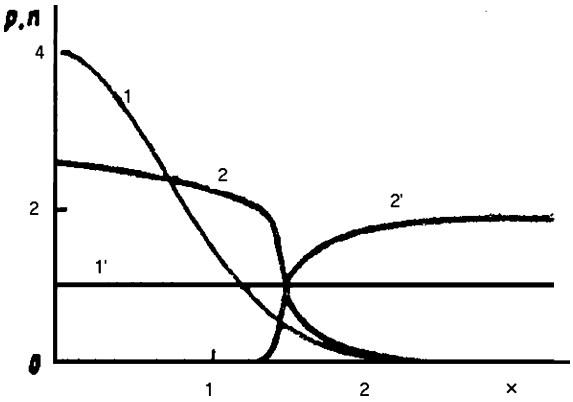

Fig. 2.5 Temporal evolution of the two positive species [32]. The ratio of ion mobilities is 0.1. Initially, the density profile of the plasma species with a large mobility was uniform (denoted by 1′) and the localized addition of a less mobile species was added (denoted by 1). After evolution in the self-consistent electric field, the mobile species (denoted by 2′) flows away from the less mobile species (denoted by 2) and they self-separate

the theoretical predictions, $u_{\text{eff}}(n_n/n_e)$ is inversely proportional to electronegativity (see (2.17)) and the regions of small negative ion density move faster than regions of large negative ion density. As a result, the front of the profile spreads out, and the back of the negative ion density profile steepens, leading to profile breaking and the formation of an ion density discontinuity – *ion density fronts*. Note that negative ion density fronts are formed at the back of the profile in contrast to gas dynamic shocks which are formed at the front of the profile. This is again due to the fact that $u_{\text{eff}}(n_n/n_e)$ is a decreasing function of electronegativity, n_n/n_e.

The effect of self-separation can also occur in multicomponent plasmas with two species of positive ions, as shown in Fig. 2.5. For this effect to occur, the two species

should have very different ion mobilities and the electron temperature should be much greater than the ion temperature. In this case ion diffusion does not spread out the two species significantly. If a large ion plasma perturbation with low mobility is added on top of a uniform two-component plasma of mobile ions, the resulting self-consistent electric field accelerates both ions away from the perturbation – but the most mobile species flows outwards faster than the less mobile species and they self-separate as shown in Fig. 2.5 [32].

2.4 Afterglow in Multicomponent Plasmas and Consequent Wall Fluxes of Negative Ions

In the previous section, it was shown that negative ions are trapped in a plasma by the self-consistent electric field. An important practical question is whether there is a way to extract negative ions from the plasma. One way to do so is to apply an external magnetic field to reduce the electron mobility near the extracting electrodes, as is done in negative ion beam sources [7]. Another approach is to extract negative ions during the afterglow, when electrons eventually leave the plasma. We pose and answer the following question: when do negative ions start reaching the walls and how big are the wall fluxes in the afterglow. The analysis of this problem was performed in [22, 23, 35–37]. When the discharge current is switched off, the electron temperature rapidly drops to room temperature and, consequently, the electron and ion temperatures equilibrate, $T_e = T_i$. Subsequently, ion diffusion becomes the dominant process. At the end of the afterglow phase of a pulsed discharge, the negative ions that accumulated in the discharge center diffuse toward the wall (see evolution of the negative ion profile at 60–600 μs in Fig. 2.2). Interestingly, if volumetric losses due to ion–ion recombination are small compared to wall losses, the solution becomes self-similar, in which all profiles are geometrically similar [38, 39]:

$$\frac{n_n(x,t)}{n_n(0,t)} = \frac{n_p(x,t)}{n_p(0,t)} = \frac{n_e(x,t)}{n_e(0,t)} = f\left(\frac{x}{\Lambda}\right), \tag{2.18}$$

where $f(x/\Lambda) = \cos(x/\Lambda)$ for slab geometry and $f(r/\Lambda) = J_0(r/\Lambda)$ for cylindrical geometry, J_0 is the Bessel function, and $x = 0$ corresponds to the center of the discharge.

Substituting the self-similar solution for plasma profiles (2.18) into the equation for the positive ion density, (2.9) yields

$$\frac{\partial n_p}{\partial t} = -\frac{\partial}{\partial x}\left(-2D_p\frac{\partial n_n}{\partial x}\right), \tag{2.19}$$

that is, the positive ions diffuse to the wall with the ambipolar diffusion coefficient, which is twice as large as that of free ion diffusion for the case of equal ion and electron temperatures. The solution of (2.19) is

$$n_p(x,t) = n_p(0,t)\,f(x/\Lambda)e^{-2t/\tau_d}, \tag{2.20}$$

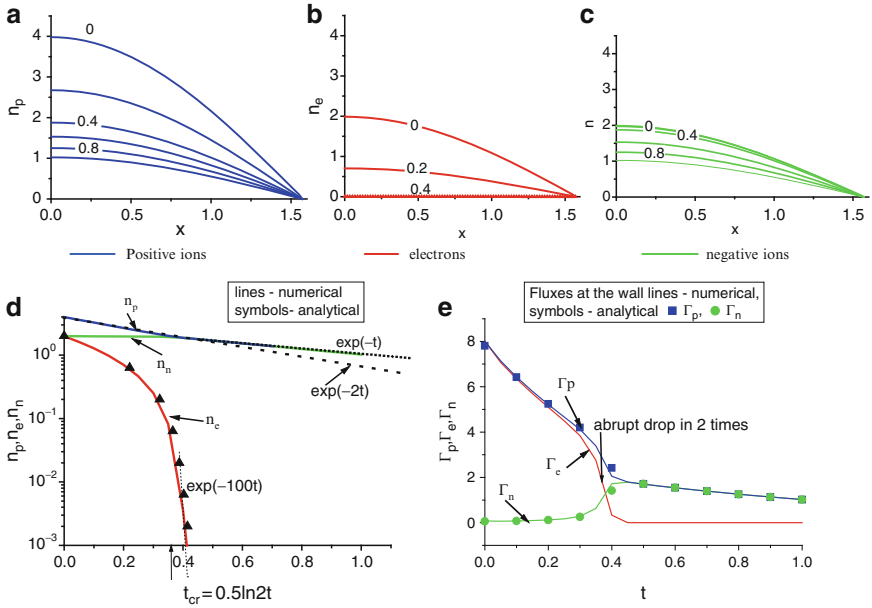

Fig. 2.6 Evolution of plasma profiles in the afterglow after the electron and ion temperatures equilibrate and establish a self-similar solution. Positive ion density (**a**), electron density (**b**), and negative ion density (**c**) profiles are plotted every 0.2 units of dimensionless time $\Lambda^2/\mu_n T_e$ [22,23]. Ion mobilities were taken to be the same. The initial profiles at $t = 0$ were taken according in accordance with to the fundamental diffusion mode of (2.18), and plasma chemical processes were neglected in the afterglow. Plasma parameters versus dimensionless time: *solid lines* are numerical results and *symbols* are analytic estimates

where $\tau_d = \Lambda^2/\mu_p T$, as shown in Fig. 2.6d. Note that such diffusion is independent of the electron density and occurs even if the electron density is much smaller than the positive ion density. Substituting the self-similar solution for plasma profiles (2.18) into the equation for the negative ion density (2.11), one obtains the result that the negative ion flux exactly vanishes, $\Gamma_n = 0$, and the negative ion density profile remains unchanged as is evident in Fig. 2.6c while electrons are present. Because the negative ions are trapped inside the plasma, the quasineutrality condition yields

$$n_e(x,t) = [n_p(0,t)e^{-2t/\tau_d} - n_n(0)]f(x/\Lambda). \tag{2.21}$$

Equation (2.21) indicates that the electron density vanishes completely at certain finite time given by

$$t_{ii} = \frac{1}{2}\tau_d \ln\left(\frac{n_p(0)}{n_n(0)}\right). \tag{2.22}$$

Electrons and positive ions are lost together to the walls; and the positive and negative ion fluxes to the walls are equal, as is evident in Fig. 2.6e. Since the electron density becomes small compared with the positive ion density, the rate of electron

loss strongly increases as the electron density tends to zero, as shown in Fig. 2.6d. Eventually the electron density becomes so small that it cannot support the electric field sufficiently to stop free electron diffusion to the walls; and the remaining electrons leave the plasma, thus a purely ion–ion plasma develops. If the negative ion and positive ion mobilities are the same, both the positive and negative ion free diffusion fluxes are automatically the same, and the ambipolar electric field is absent for a purely ion–ion plasma. Therefore, further plasma decay occurs with the free ion diffusion rate:

$$n_{\mathrm{p}}(x,t) = n_{\mathrm{n}}(x,t) = n_{\mathrm{n}}(0,t)\, f(x/\Lambda)\mathrm{e}^{-t/\tau_{\mathrm{d}}}. \tag{2.23}$$

Experimental measurements of the wall fluxes [40] shown in Fig. 2.6e agree well with the analytic description outlined earlier.

In the description of temporal plasma decay in an afterglow we neglected volumetric processes in the plasma. Generalization of these results taking into account attachment and detachment processes is straightforward and is described in [22, 23, 35]. The most important qualitative effect occurs due to detachment and production of electrons from negative ions. If the detachment frequency, γ_{d}, is faster than the ambipolar wall loss frequency (see (2.20)):

$$\gamma_{\mathrm{d}} > 2/\tau_{\mathrm{d}}. \tag{2.24}$$

The attached electrons are produced quickly enough by this mechanism so that electrons are always present in the afterglow. Therefore, the negative ions are always trapped in this case. Because the detachment rate is proportional to the gas pressure, but the diffusion coefficient is inversely proportional to the gas pressure, increasing pressure can lead to a sudden transition from the regime in which detachment is small to the regime in which the detachment frequency dominates the wall losses and the criterion condition in (2.24) is satisfied. The trapping of negative ions throughout afterglow is demonstrated in Fig. 2.7 for pressures higher than 3.5 mTorr.

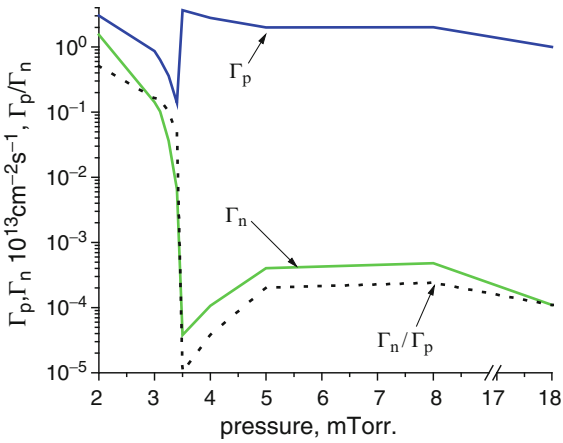

Fig. 2.7 Maximum negative ion flux in the oxygen afterglow as a function of pressure [35]. The discharge interelectrode gap is 10 cm and average power density is 10 mW/cm^3

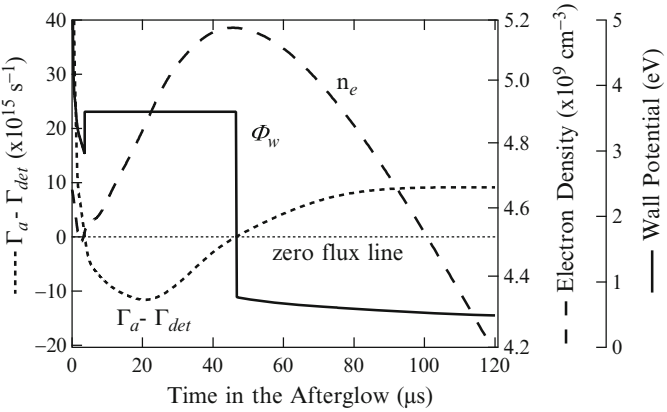

Fig. 2.8 The electron density, the wall potential, and the electron temperature evolution in the afterglow of discharge in oxygen [42]. Calculated difference between the ion flux Γ_a and the electron flux available from negative ion detachment Γ_{det} is shown on the *left*; the electron density and the calculated wall potential are shown on the *right*

Note also that associative detachment of electrons can lead to creation of free electrons with energies much larger than the representative average energies of electrons and ions in afterglow (which can be typically close to the room temperatures). For instance, in oxygen reaction $O^- + O \rightarrow O_2 + e$, the energy of generated electrons can be up to 3.6 eV. Due to this process, walls of the plasma volume can be charged negatively up to −3.6 V in the above example. Without the presence of the fast electrons, one would normally expect the electron density, the wall potential and the electron temperature to monotonically decrease. However, during the afterglow, a sharp change in sheath voltage drop is possible due to generation of the fast electrons, as described in [41]. For an example, Fig. 2.8 shows the electron density, the wall potential and the electron temperature evolve non-monotonically in the afterglow of discharge in oxygen. It is evident from Fig. 2.8 that the electron density initially decreases, then increases for a time between 3 and 45 μs, and then decreases again. This increase corresponds to the time interval in which electrons are trapped by the high wall potential, which is also shown in the figure. The wall potential is determined by the difference between the ion flux to the wall and the available flux of the fast electrons generated due to associative detachment in oxygen [42]. We can see that during the time between 3 and 45 μs, the difference in those fluxes is negative, that is, the available flux of fast electrons is large compared with the flux of ions. As a result, all thermal electrons and a portion of the fast group are trapped during this part of the afterglow to satisfy ambipolarity condition.

2.5 Steady-State Profiles of Plasmas with Negative Ions

Examples of measured and simulated density positional profiles in plasmas with the addition of negative ions are shown in Figs. 2.9–2.11.

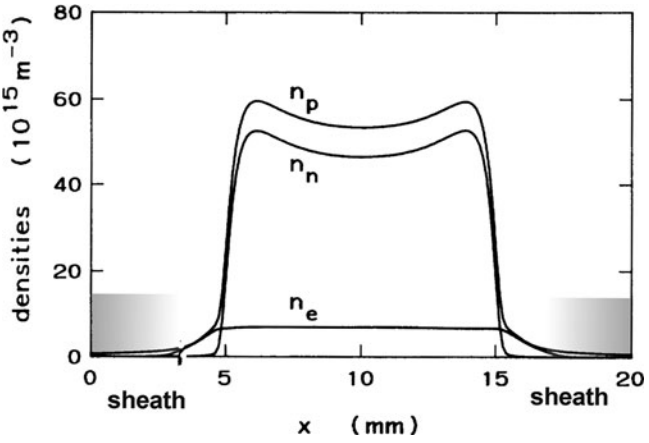

Fig. 2.9 Plasma profiles in rf-discharge, 0.5 Torr CF4, 13.6 MHz [43]. Shaded region marks sheath

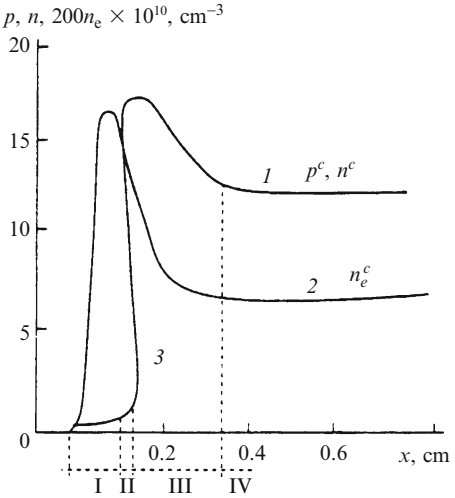

Fig. 2.10 Profiles of the charged particle densities obtained in simulations of rf-discharge in SF_6 [45]. The trace 1 corresponds to the positive and negative ion densities, and trace 2 to the time-averaged electron density. The discharge parameters are the gas pressure 0.13 Torr, rf-frequency 13.6 MHz, and current density 2 mA/cm^2. Region I corresponds to the sheath, region III to the ion density perturbation associated with the sheath, region IV is a region of nearly uniform ion density profile in the plasma bulk, and region II is the narrow transition region between regions I and III where negative ion density jumps

The common feature of all profiles is that the plasma tends to stratify into a bulk plasma region where the negative ion density is larger than the electron density and a peripheral region near the sheath where the electron density is large compared with the negative ion density. (A notable exception is the case of a very strongly

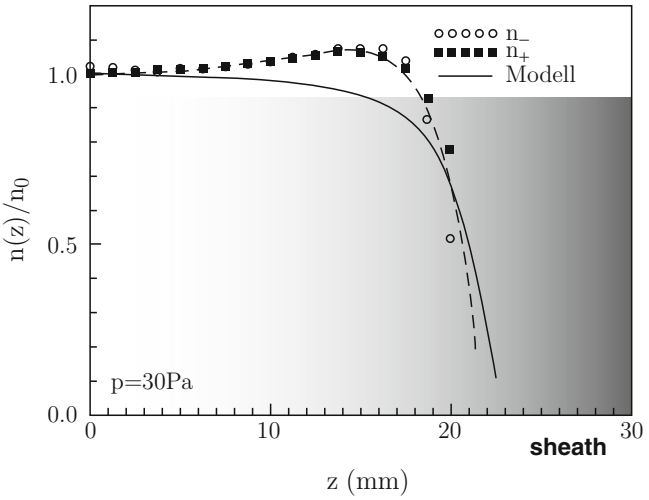

Fig. 2.11 Experimentally measured and simulated negative ion density profiles in an rf-discharge in oxygen, pressure 0.21 mTorr [44]. The central ion density is 3.5×10^9 cm^{-3} and the electron density profile is nearly uniform with density 1.5×10^8 cm^{-3}. Shaded region marks the sheath

electronegative gas, SF_6, shown in Fig. 2.10.) In the sheath region, the electric field accelerates negative ions toward the plasma center. The negative ion flux increases toward the plasma center due to attachment. As shown in Sect. 2.3, the negative ion flow velocity decreases as soon as the negative ion density becomes large compared with the electron density. At this point the negative ion density increases sharply forming a distinct boundary between the electropositive peripheral region, in which $n_n/n_e < 1$ and the electronegative core with $n_n/n_e \gg 1$, as shown, for example, in Fig. 2.9.

An analytic calculation of the exact width of the electropositive peripheral region requires an accurate calculation of the negative ion flux and ion velocity, which can be affected by the number of processes included in simulations of realistic plasma profiles: for example, accounting for finite ion mean free path, effects of ion diffusion and width of the sheath region. These will not be described here; see [3,17,20,21,25–30,33,44,46] for details. However the central region should satisfy a simple relation between ion and electron densities. In the bulk plasma ion diffusion can be neglected and the positive and negative ion fluxes become mostly convective $\Gamma_p \approx \mu_p e n_p E$ and $\Gamma_n \approx -e\mu_n n_n E$. As the negative ion density becomes large, $n_n/n_e \gg 1$, the ion fluxes should be nearly equal, $\mu_n\Gamma_p + \mu_p\Gamma_n \approx 0$ as shown in Fig. 2.12. Because of this $\mu_n \partial\Gamma_p/\partial x + \mu_p \partial\Gamma_n/\partial x \approx 0$, and the sources of positive and negative ions have to satisfy the relation

$$\mu_n S_p + \mu_p S_n \approx 0. \tag{2.25}$$

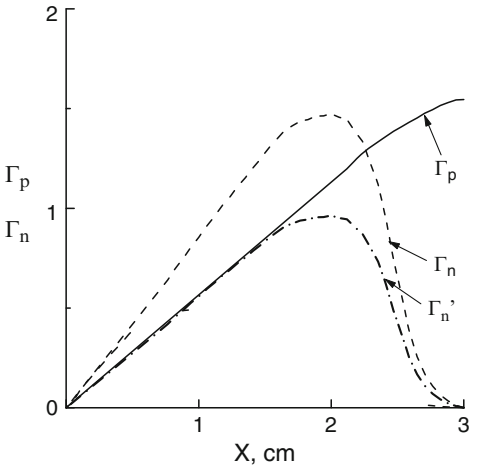

Fig. 2.12 Calculated ion fluxes in units of $10^{13}\,\mathrm{cm}^2/\mathrm{s}$ for the same parameters as in Fig. 2.11. *Dashed lines* represent negative ion fluxes. The *line* marked as Γ_n' corresponds to the negative ion flux divided by $D_n/D_p = 1.4$

For a typical electronegative gas, positive ion production is due to ionization and loss is due to ion–ion recombination, $S_p = Z_{iz} n_e - \beta_{ii} n_n n_p$; negative ion production is due to electron attachment and loss due to ion–ion recombination and detachment, $S_n = \alpha_{at} n_e - \gamma_d n_n - \beta_{ii} n_n n_p$. Substituting these equations for the positive and negative ion production rates into (2.25) yields [12, 20, 21, 24–30, 44, 47]

$$\left(\frac{\mu_n}{\mu_p} Z_{iz} + \alpha_{at}\right) n_e - \gamma_d n_n \approx \left(1 + \frac{\mu_n}{\mu_p}\right) \beta_{ii} n_n n_p. \tag{2.26}$$

This relation was verified for the positive and negative ion and electron densities for the conditions of Figs. 2.8–2.10.

2.6 The Sheath in Strongly Electronegative Gases

The properties of a sheath in strongly electronegative plasmas can be even more complicated than the properties of quasineutral plasmas. Walls and rf-electrodes are charged negatively by the plasma to provide an ambipolarity condition for the electron and ion fluxes to the walls. Therefore, negative ions are driven toward the plasma center inside the sheath region. In an rf-discharge the electric field at the electrode is modulated in time and the plasma sheath boundary moves toward and away from the electrode in accord with the electric field variations. When the electric field decreases, electrons move closer to the electrode and during this phase they can produce negative ions due to attachment inside the rf-sheath. Ions are much slower compared with the electrons and cannot respond to the instantaneous electric field, and thus respond to a time-averaged electric field, which always pushes

them toward the plasma center. In this averaged electric field negative ions gain velocity and drift toward the center. Their flux increases due to electron attachment and their velocity decreases toward the plasma sheath boundary. If the product of the frequency of attachment, ν_{at} times the time for a negative ion to traverse the sheath region, $\tau_i \sim L_{sh}/V_i$, is small compared with unity, $\nu_{at}\tau_i < 1$, the negative ion density in the sheath is small compared with the electron density and the sheath structure is not affected by the negative ions. In the opposite case, $\nu_{at}\tau_i \gg 1$, negative ion production is so strong that the presence of negative ions strongly modifies the sheath structure. As the attachment frequency increases, the negative ion density also increases inside the sheath region and so does the positive ion density. Analysis of the transport equations shows that in this case the electron density inside the sheath can greatly exceed the electron density in the bulk plasma, as is evident in Fig. 2.10. As a result, the sheath width is greatly reduced and, as shown in [48], the sheath region self-consistently adjusts itself to satisfy the condition $\nu_{at}\tau_i \approx 1$. The positive ion density jumps at the end of the sheath due to fast ion deceleration. Under certain conditions, such a rapid increase of ion density can also produce sharp peaks in ion density as shown in Fig. 2.13. For a detailed description of these effects, see [18, 48].

The presence of negative ions in rf-discharges can result in a number of other complicated nonlinear phenomena, like the generation of low-frequency oscillations corresponding to the sheath restructuring from cathode-like to anode-like structures [49] and the generation of $f/3$ and $2f/3$ harmonics [45], where f is the discharge frequency.

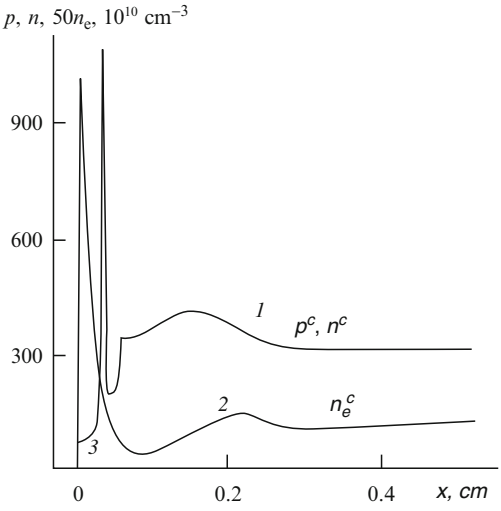

Fig. 2.13 The formation of ion density peaks in the simulation [45]. The conditions are the same as those of Fig. 2.10 except for higher pressure (1.33 Torr) and current (100 mA/cm^2)

2.7 The Connection Between Plasmas with Negative Ions, Dusty Plasmas, and Ball Lightning

Particles are often formed in processing plasmas and they affect plasma properties. Deliberate synthesis of nanoparticles is used in applications ranging from photovoltaics to cancer treatment. As will be described below, the presence of small particles may also explain the properties of ball lightning. When particles are very small, about a nm in diameter, most of them have charge zero or ± 1, with the particle charging process dominated by stochastic fluctuations. Larger particles are always charged negatively due to the large incoming electron flux incident on the particle. Negatively charged particles act as negative ions and are pushed to the center of the plasma by the electric field. Charged species' profiles in dusty plasmas are shown in Fig. 2.14 [50,51]. The formation of large ion and particle density gradients is apparent inside the plasma, similar to the negative ion density fronts described in Sect. 2.5. For larger particles ion drag has to be taken into account as well as the electric field. When the particle size increases even further the ion drag overcomes the force due to the electric field and pushes the particles out of the center, producing a void. This void has been observed to undergo a "heartbeat instability," in which it periodically expands and contracts [52]. Further details about particle transport and dynamics can be found in Chaps. 7 and 9.

Here, we only wish to point out the connection of negative ions and negatively charged microparticles to ball lighting, photographs of which are shown in Fig. 2.15. A remarkable feature of ball lightning reported by observers is that it resumes a rounded shape after colliding with an obstacle and even in passing through an

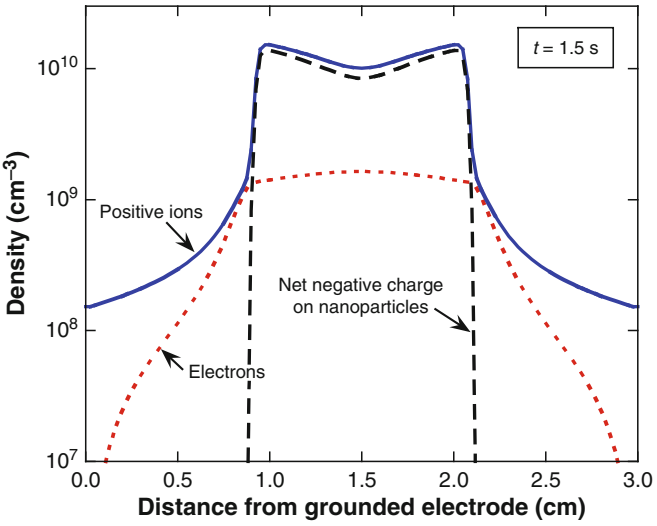

Fig. 2.14 Predicted profiles of charge carrier densities at 1.5 s following onset of nucleation, with particle size about 20 nm [48]

Fig. 2.15 Photographs of ball lightning (from http://www.zeh.ru/shm/index_e.php)

Fig. 2.16 Photograph of a fireball in a microwave drill (from [54])

aperture. There were many attempts to reproduce ball lightning in the laboratory, most notably the recent experimental studies of [53, 54]. Jerby and Dikhtyar [53] produced a fireball resembling ball lightning in an industrial microwave drill. The *Nature* article [55] comments that "Such fire balls (pictured in Fig. 2.16) mimic two of the most perplexing aspects of ball lightning – they persist after the initial source of energy is removed and they float in air. This supports previous suggestions that ball lightning could be driven by the oxidation of particles in a cloud generated by an energetic event, such as a conventional lightning strike." In previous experiments including that of [53], fireballs extinguished almost immediately after the discharge power was switched off (Fig. 2.16). In contrast to these previous experiments, Paiva et al. [54] performed electric arc discharges in pure silicon and were able to generate luminous balls with a lifetime of the order of seconds. The source of energy was chemical – burning of small silicon particles produced in the arc, shown in Fig. 2.17.

The presence of a large number of silicon particles in the plasma of a fireball was verified recently by small-angle X-ray scattering [56]. The authors claim that "The results show that the fireballs contain particles with a mean size of $\sim$50 nm with

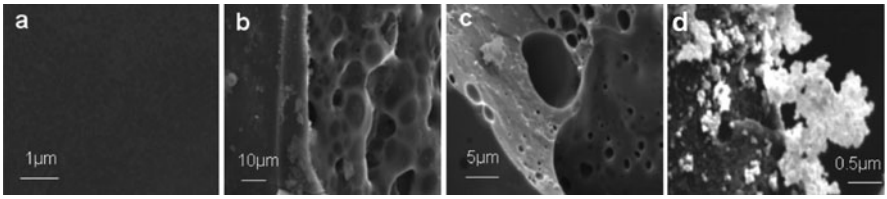

Fig. 2.17 SEM of the Si wafer before (**a**) and after electrical discharge (**b**)–(**d**). The surface of the samples subjected to electrical discharges shows holes (**b**, **c**) and chains of micrometer-sized particles (**d**) (from [54])

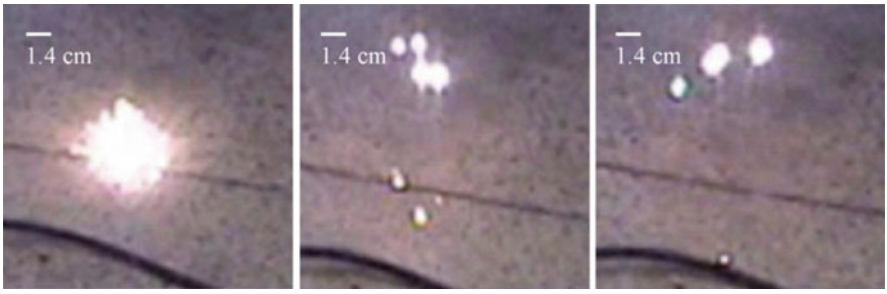

Fig. 2.18 Successive video frames showing the luminous balls bouncing off the ground. Time interval between the frames is 80 ms (from [54]). See also the supplementary video 2 (from [58])

average number densities on the order of $\sim 10^9$. Hence, fireballs can be considered as a dusty plasma which consists of an ensemble of charged nanoparticles in the plasma volume" [56]. All these findings give support to the Abrahamson–Dinniss theory for the formation of ball lightning [57] based on the generation of an oxidizing silicon particle network liberated by lightning striking the ground.

As explained in Sects. 2.4 and 2.5, the self-consistent electric field in a plasma $\vec{E} = -T_e \vec{\nabla} \ln n_e$ pushes negatively charged particles into the plasma center. If ball lightning or fireballs are supported by the burning of dust particles, such coupling between plasma production and transport may explain the tendency of these objects to resume a rounded shape, because all the negative ions move toward the plasma density maximum, thus acting as an effective surface tension. An example of such an event restoring the rounded shape of a fireball is shown in Fig. 2.18 (taken from [54]).

In summary, the presence of negative ions makes plasma transport much more complicated and interesting. Many complex nonlinear phenomena remain to be explained.

Acknowledgments The authors are thankful for stimulating discussions with Norman J.M. Horing, Larry Grisham, Lev D. Tsendin, and Alan J. Lichtenberg. This work was partially supported by the Air Force Office of Scientific Research through STTR Phase 2 contract.

References

1. H.S.W. Massey, *Negative Ions* (Cambridge University Press, Cambridge, 1974)
2. B.M. Smirnov, *Negative Ions* (McGraw-Hill, New York, 1982)
3. M.A. Lieberman, A.J. Lichtenberg, *Principles of Plasma Discharges and Materials Processing, 2nd edn.* (Wiley, New York, 2005)
4. G.S. Hwang, K.P. Giapis, Phys. Rev. Lett. **79**, 845 (1997)
5. W. Swider, *Ionospheric Modeling* (Birkhauser, Basel, 1988)
6. I M. Kuriyama et al., Fusion Eng. Des. **39–40**, 115 (1998)
7. L.R. Grisham, Nucl. Instrum. Methods Phys. Res. A **464**, 315 (2001)
8. A.A. Howling, I. Sansonnens, J.-L. Dorier, C. Hollenstein, J. Phys. D Appl. Phys. **26**, 1003 (1993)
9. N.L. Aleksandrov, A.P. Napartovich, Sov. Phys. Uspekhi **36**, 107 (1993)
10. B.M. Smirnov, *Physics of Ionized Gases* (Wiley-IEEE, New York, 2001), p. 165
11. P.P. Raizer, *Gas Discharge Physics* (Springer, Berlin, 1991)
12. V.A. Rozhansky, L.D. Tsendin, *Transport Phenomena in Partially Ionized Plasma* (CRC, Boca Raton, 2001)
13. I.G. Kouznetsov, A. Lichtenberg, M. Lieberman, Plasma Sci. Technol. **5**, 662 (1996)
14. I.G. Kouznetsov, A. Lichtenberg, M. Lieberman, J. Appl. Phys. **86**, 4142 (1999)
15. V.I. Kolobov, D.J. Economou, Appl. Phys. Lett. **72**, 656 (1998)
16. P. Chabert, A.J. Lichtenberg, M.A. Lieberman, Phys. Plasmas **14**, 093502 (2007)
17. I.D. Kaganovich, L.D. Tsendin, IEEE Trans. Plasma Sci. **20**, 66 (1992)
18. I.D. Kaganovich, L.D. Tsendin, N.A. Yatsenko, Sov. Phys. Tech. Phys. **39**, 1215 (1994)
19. A.P. Dmitriev, V.A. Rozhansky, L.D. Tsendin. Sov. Phys. Uspekhi **28**, 467 (1985)
20. R.N. Franklin, Plasma Sour. Sci. Technol. **11**, A31 (2002)
21. R.N. Franklin, J. Phys. D Appl. Phys. **36**, 828 (2003)
22. I.D. Kaganovich, D.J. Economou, B. Ramamutri, V. Midha, Phys. Rev. Lett. **84**, 1918 (2000)
23. I.D. Kaganovich, B. Ramamutri, D.J. Economou, Phys. Rev. E **64**, 036402 (2001)
24. L.D. Tsendin, Sov. Phys. Tech. Phys. **34**, 11 (1989)
25. C. Ferreira, G. Gousset, M. Touseau, J. Phys. D Appl. Phys. **21**, 1403 (1988)
26. C. Ferreira, G. Gousset, J. Phys. D Appl. Phys. **24**, 775 (1991)
27. P.G. Daniels, R.N. Franklin, J. Phys. D Appl. Phys. **22**, 780 (1989)
28. P.G. Daniels, R.N. Franklin, J. Snell, J. Phys. D Appl. Phys. **23**, 823 (1990)
29. R.N. Franklin, P.G. Daniels, J. Snell, J. Phys. D Appl. Phys. **26**, 1638 (1993)
30. R.N. Franklin, J. Snell, J. Phys. D Appl. Phys. **27**, 21823 (1990)
31. I.D. Kaganovich, Phys. Plasmas **8**, 2540 (2001)
32. I.D. Kaganovich, L.D. Tsendin, Plasma Phys. Rep. **19**, 645 (1993)
33. I. Kaganovich, S.V. Berezhnoi, C.B. Shin, Phys. Plasmas **8**, 719 (2001)
34. G.B. Whitham, *Linear and Nonlinear Waves* (Wiley, New York, 1974)
35. I.D. Kaganovich, B.N. Ramamurthi, D.J. Economou, Appl. Phys. Lett. **76**, 284 (2000)
36. E.A. Bogdanov, A.A. Kudryavtsev, L.D. Tsendin, Tech. Phys. Lett. **27**, 652 (2001)
37. E.A. Bogdanov, A.A. Kudryavtsev, L.D. Tsendin, Tech. Phys. **46**, 404 (2001)
38. M.V. Koniukov, Sov. Phys. JEPT **12**, 629 (1958)
39. A.V. Phelps, J. Res. Natl. Inst. Stand. Technol. **95**, 407 (1990)
40. D. Smith, A.G. Dean, N.G. Adams, J. Phys. D Appl. Phys. **7**, 1944 (1974)
41. V.I. Demidov et al., Phys. Rev. Lett. **95**, 215002 (2005)
42. C.A. DeJoseph Jr. et al., Phys. Plasmas **14**, 057101 (2007)
43. J.D. Passchier, W.J. Goedheer, J. Appl. Phys. **73**, 1073 (1993)
44. S.V. Berezhnoi, U. Buddemeier, I. Kaganovich, C.B. Shin, Appl. Phys. Lett. **77**, 800 (2000)
45. V.A. Schweigert, Plasma Phys. Rep. **17**, 844 (1991)
46. A.J. Lichtenberg, I.G. Kouznetsov, Y.T. Lee, M.A. Lieberrman, I.D. Kaganovich, L.D. Tsendin, Plasma Sour. Sci. Technol. **6**, 437 (1997)
47. M. Lampe, W.M. Manheimer, R.F. Fernsler, S.P. Slinker, G. Joyce, Plasma Sour. Sci. Technol. **13**, 15–26 (2004)

48. I.D. Kaganovich, Plasma Phys. Rep. **21**, 434 (1995)
49. Y.P. Raizer, M.N. Shneider, N.A. Yatsenko, *Radio Frequency Capacitive Discharges* (CRC, Boca Raton, 1995)
50. L. Ravi, S.L. Girshick, IEEE Trans. Plasma Sci. **36**, 1022 (2008)
51. S.J. Warthesen, S.L. Girshick, Plasma Chem. Plasma Process. **27**, 292 (2007)
52. M. Mikikian, L. Boufendi, Phys. Plasmas **11**, 3733 (2004)
53. E. Jerby, V. Dikhtyar, Phys. Rev. Lett. **96**, 045002 (2006)
54. G.S. Paiva et al., Phys. Rev. Lett. **98**, 048501 (2007)
55. Nat. Phys. 2 March 2006 Research Highlights Great balls of fire!
56. J.B.A. Mitchell, J.L. LeGarrec, M. Sztucki, T. Narayanan, V. Dikhtyar, E. Jerby, Phys. Rev. Lett. **100**, 065001 (2008)
57. J. Abrahamson, J. Dinniss, Nature (Lond.) **403**, 519 (2000)
58. See EPAPS Document No. E-PRLTAO-98-047705 for video clips showing the experiment and the luminous balls. For more information on EPAPS, see http://www.aip.org/pubservs/epaps.html

http://www.springer.com/978-3-642-10591-3

Introduction to Complex Plasmas

Bonitz, M.; Horing, N.; Ludwig, P. (Eds.)
2010, XVIII, 450 p. 225 illus., 76 illus. in color.,
Hardcover
ISBN: 978-3-642-10591-3